



Activating BaTaO₂N by Ca modifications and cobalt oxide for visible light photocatalytic water oxidation reactions

Shunhang Wei^a, Guan Zhang^{b,*}, Xiaoxiang Xu^{a,*}

^a Shanghai Key Lab of Chemical Assessment and Sustainability, School of Chemical Science and Engineering, Tongji University, 1239 Siping Road, Shanghai, 200092, China

^b School of Civil and Environmental Engineering, Harbin Institute of Technology, Shenzhen 518055, China

ARTICLE INFO

Keywords:

BaTaO₂N

Photocatalysis

Visible light photocatalyst

Water oxidation

Cocatalyst

ABSTRACT

Despite a strong visible light absorbance as far as 660 nm, BaTaO₂N generally exhibits a poor photocatalytic activity for water splitting under ordinary conditions. High levels of defects as well as photocatalytic self-decomposition are likely the major causes for this incommensuration. In this work, we have modified BaTaO₂N by introducing Ca to the structure, i.e. BaCa_{x/3}Ta_{1-x/3}O_{2+y}N_{1-y} (0 ≤ x, y ≤ 1). A number of important properties such as band gap, defects levels and nitrogen content can be tuned by varying the amounts of Ca in the structure. In particular, defects such as Ta⁴⁺ species can be effectively suppressed by Ca incorporation. More importantly, photocatalytic activity for water oxidation has been significantly enhanced and stability against photocatalytic self-decomposition has also been largely improved in Ca modified BaTaO₂N. An apparent quantum efficiency as high as ~ 2.1% at 420 ± 20 nm has been achieved and stands as the highest AQE for BaTaO₂N reported to date. Photoelectrochemical (PEC) analysis reveals a much higher photocurrent in Ca modified BaTaO₂N and identifies the role of cocatalyst CoO₂ in reducing charge transfer resistance for water oxidation reactions. Open-circuit voltage decay (OCVD) measurements further confirm the improved charge separation conditions in Ca modified BaTaO₂N and functions of cocatalyst CoO₂ in collecting and storing photo-generated holes. The optimal loading point for cocatalyst CoO₂ corresponds to the one that gives the highest capacity for hole storage.

1. Introduction

The limited reservoirs of fossil fuels on this planet and various environmental issues linked to fossil fuel consumptions pose critical challenges to the sustainability of our modern economies [1–4]. An appealing strategy to combat these challenges and more importantly, to free us from fossil fuel reliance is solar water splitting into hydrogen and oxygen on particulate semiconductors [5–9]. This is not only because hydrogen is a clean energy vector whose cycling involves only water but also because solar irradiation is inexhaustible and widely accessible all over the world [10,11]. Although decades of efforts have been devoted to searching and developing efficient photocatalysts, very few compounds/systems demonstrate solar to hydrogen efficiency high enough to win commercial interest [12–15]. This is at least partially due to the complexity of solar water splitting reactions which involves light absorption, charge separation, water reduction/oxidation processes etc. on a single particle [16]. Breakthrough on the efficiency of solar water splitting therefore relies on meticulous management of these processes so that optimization at each step is achieved [17]. In particular, water oxidation is a four-proton-four-hole reaction, being

energetically and mechanistically difficult [18–21]. Thereby, semiconductors that are capable of water oxidation with appreciable visible light absorption are strongly desired. In this regard, a number of perovskite oxynitrides have gained considerable attention not only due to their strong visible light absorption but also because of their thermodynamic feasibility for photocatalytic water oxidation reactions [22–26]. Nevertheless, efficient photocatalytic water splitting is hardly achieved on these materials, being incommensurate to their strong visible light absorption. For instance, perovskite oxynitrides AMO₂N (A = Ca, Sr and Ba; M = Nb and Ta) produce little amounts of oxygen from water under ordinary conditions [27–35] and photocatalytic self-decompositions are occasionally seen even under protection of a hole scavenger [29,30]. Various types of defects produced during synthetic procedures (involving high temperature and ammonia) are likely the major reason as they not only lower down crystal integrity but also induce fast charge recombination events that rapidly dissipate photo-generated charges [20,21,36–38]. Therefore, methods to control defects levels within these perovskite oxynitrides are promising to activate their photocatalytic performance [36,39]. More importantly, band gap/edges tailoring of a semiconductor is highly useful in photocatalytic

* Corresponding authors.

E-mail addresses: zhangguan@hit.edu.cn (G. Zhang), xxu@tongji.edu.cn (X. Xu).

systems (e.g. Z-scheme, heterojunctions etc.), photoelectrochemical setup (e.g. tandem cell) or dyes/pigment industries where light absorption or charge migration needs to be manipulated [40–45]. Adjustment of optical properties/electronic structures of the perovskite oxynitrides without altering their perovskite structure are quite beneficial for those applications [24,46–48]. Previous study on BaTaO₂N with doped cations such as W, Ba, Zr, etc have gained some success on improving the photocatalytic activity yet problems still exist such as high defects levels [35,49–51]. In this work, we have introduced Ca into the B site of BaTaO₂N, i.e. BaCa_{x/3}Ta_{1-x/3}O_{2+y}N_{1-y} ($0 \leq x, y \leq 1$), and successfully gained control over its defects levels (e.g. Ta⁴⁺ species) and band gap. More interestingly, compared to pristine BaTaO₂N, nearly 3-fold enhancement in photocatalytic oxygen production has been achieved in Ca modified BaTaO₂N. The underlying mechanism for such improvement as well as interactions between cocatalyst CoO₂ and Ca modified BaTaO₂N have also been investigated. This simple strategy adopted in this work signifies how a slight composition modification in perovskite oxynitrides is applicable to design optical and photocatalytic properties.

2. Experimental

2.1. Materials preparation

Ca modified BaTaO₂N (BaCa_{x/3}Ta_{1-x/3}O_{2+y}N_{1-y} ($0 \leq x, y \leq 1$)) was prepared via a polymerized complex method: stoichiometric amounts of Ba(NO₃)₂ (SCR, 99.5%), calcium nitrate tetrahydrate (Aladdin, 99%), TaCl₅ (Alfa Aesar, 99.99%) and 3 g anhydrous citric acid (Aladdin, 99.5%) were added into 10 ml ethylene glycol (Aladdin, 98%). The mixtures were magnetically stirred at 423 K on a hotplate until a transparent solution was formed. The temperature was then raised to 573 K to promote polymerization until brown resin appeared. The resin was subsequently calcined at 823 K for 20 h for the removal of organic species and white powder-like precursor was obtained. The precursor was transferred into an alumina boat and mounted in a tube furnace for ammonolysis. Ultrapure ammonia gas (Jiaya Chemicals, 99.999%) was directed into the tube furnace at a flowing rate of 250 ml min⁻¹. The furnace was ramped to 1273 K and dwelled on this temperature for 15 h and naturally cooled to room temperature. The resultant powders were collected for further analysis. The variable x in the formula BaCa_{x/3}Ta_{1-x/3}O_{2+y}N_{1-y} ($0 \leq x, y \leq 1$) is controlled by varying the Ca/Ta molar ratios in the initial precursors.

2.2. Materials characterization

The crystal structure and phase purity of as-prepared sample powders were analyzed using X-ray powder diffraction (XRD) techniques on a Bruker D8 Focus diffractometer. Incident radiations are Cu K_{α1} ($\lambda = 1.5406 \text{ \AA}$) and Cu K_{α2} ($\lambda = 1.5444 \text{ \AA}$). Typical step size and duration time for data collection are 0.01° and 0.1 s. Unit cell parameters and other structure information were examined by performing Rietveld refinement on XRD data using the General Structure Analysis System (GSAS) software package [52]. Optical properties were examined on a UV–vis spectrophotometer coupled with an integrating sphere (JASCO-750). All data were analyzed using JASCO software suite. BaSO₄ was used as a reference non-absorbing material [53]. A field emission scanning electron microscope (Hitachi S4800) was used to inspect the microstructures of freshly prepared samples. Surface conditions of as-prepared sample powders were evaluated by X-ray photoelectron spectroscopy (Thermo Escalab 250 with a monochromatic Al K_α X-ray source). All bonding energies were adjusted according to adventitious carbon C 1s peak at 284.7 eV [54]. The surface area of as-prepared samples was analyzed on a Micro-meritics instrument TriStar 3000 and were calculated based on the Brunauer-Emmett-Teller (BET) model. Nitrogen content within samples was calculated from thermogravimetric analysis (TGA) in air ramping from room temperature to 1300 °C.

2.3. Photocatalytic water oxidation

Photocatalytic water oxidation into O₂ was performed in a top-irradiation-type reactor linked to a gas-closed circulation and evacuation system (Perfect Light, Lab solar-III A). The temperature of the reactor was stabilized by a water jacket at 293 K. In a typical experiment, 100 mg sample powders were ultrasonically dispersed into 100 ml AgNO₃ aqueous solution (0.01 M). The so-formed suspension was sealed in the reactor and evacuated for 30 min to remove air dissolved. Proper amounts of CoO₂ were applied as a co-catalyst and were loaded onto sample powders according to previous reports [20,38,55,56]: appropriate amounts of cobalt nitrate aqueous solution were impregnated into 100 mg sample powders under magnetic stirring to form a slurry. The slurry was heated at 353 K in air until dry, calcined in flowing ammonia at 1023 K for 1 h and re-calcined in air at 423 K for another 1 h. A 300 W Xenon lamp (Perfect Light, PLX-SXE300) was used as a light source and is coupled with a UV cut-off filter ($\lambda \geq 420 \text{ nm}$) to generate visible light or an AM1.5 filter to simulate solar light irradiation. Monochromatic light irradiation was produced by filtering the output of the lamp with corresponding bandpass filters. The photon flux was calibrated using a quantum meter (Apogee MP-300). The gas within the reactor was then sampled by an on-lined GC (TECHCOMP, GC7900) with a TCD detector (5 Å molecular sieve columns and Ar carrier gas). The apparent quantum efficiency (AQE) is calculated using the following equation:

$$\text{Apparent quantum efficiency} = 4 \times \text{moles of oxygen production per hour} / \text{moles of photon flux per hour} \times 100\%$$

2.4. Photoelectrochemical (PEC) measurements

Electrophoretic deposition method was used to prepare photoelectrode for PEC measurements: two pieces of fluorine-doped tin oxide (FTO) glass (30 × 10 mm) were inserted in parallel into 50 ml acetone solution containing 40 mg sample powders and 10 mg iodine. The distance between FTO glasses was kept at 10 mm with conductive sides facing inward. A constant bias (10 V) was applied between the pair of glass pieces for 3 min under potentiostatic control (Keithley 2450 Source Meter). The powders were then gradually deposited onto the FTO glass at the anode side which was then used as a photoelectrode. The photoelectrode was calcined at 673 K for 60 min for the removal of absorbed iodine. TiCl₄ (Alfa Aesar, 99.99%) methanol solution (10 mM) was dropped onto the electrode and was dried in air. This procedure was repeated six times in order to enhance the particle connectivity and reduce the exposure of naked FTO [57]. The electrode was then calcined in N₂ flow (20 ml min⁻¹) at 673 K for 60 min. PEC experiments were performed in a three-electrode configuration using a Zahner electrochemical workstation. The sample photoelectrode, Pt foil (10 × 10 mm) and Ag/AgCl electrode were used as working, counter and reference electrodes, respectively. K₃PO₄/K₂HPO₄ aqueous solution (0.1 M, pH = 7.95) was used as an electrolyte and a buffer. A 300 W Xenon lamp (Perfect Light, PLX-SXE300) coupled with a UV cut-off filter ($\lambda \geq 420 \text{ nm}$) or an AM 1.5 filter was applied as the light source. Incident light was rectified by an electronic timer and shutter (DA-HENG, GCI-73).

3. Results and discussions

3.1. Phase purity and crystal structure

Perovskite oxynitrides are generally prepared by nitridizing proper crystallized metal oxide precursors at high temperatures, e.g. Ba₂Ta₂O₇ for the preparation of BaTaO₂N [24]. Relatively long nitridation time is often needed for the production of single phase compound [24,47]. This is mostly due to the refractory nature of these crystallized metal oxides in which ion diffusion and rearrangements are extremely slow [58]. In this work, we use amorphous precursors as alternatives to synthesize

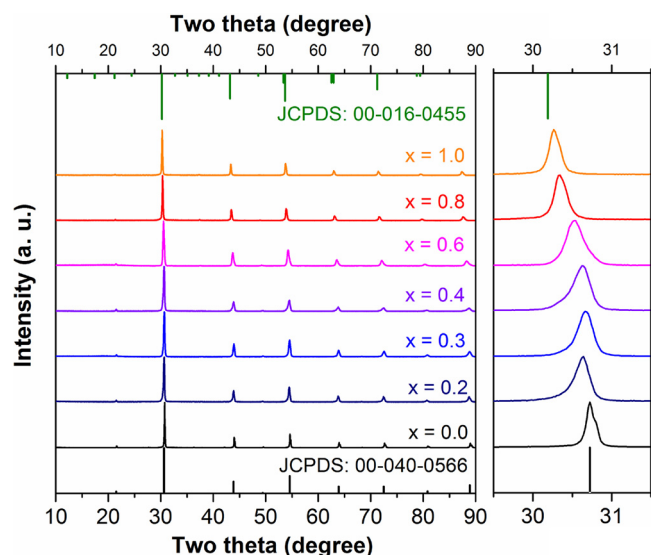


Fig. 1. X-ray powder diffraction patterns of as-prepared samples $\text{BaCa}_{x/3}\text{Ta}_{1-x/3}\text{O}_{2+y}\text{N}_{1-y}$ ($0 \leq x, y \leq 1$), (011) diffraction peak are enlarged on the right for clarity, standard XRD patterns for BaTaO_2N (JCPDS: 00-040-0566) and $\text{BaCa}_{1/3}\text{Ta}_{2/3}\text{O}_3$ (JCPDS: 00-016-0455) are also included for comparisons.

the target perovskite oxynitrides and we find they are quite helpful for single phase formation and substantially shorten the nitridation time. This can be rationalized by the fact that all ions in the amorphous precursors are homogeneously dispersed at atomic level thereby greatly reducing the thresholds for ion diffusion and rearrangement. More importantly, diverse cation ratios are allowed in amorphous precursors which offer us freedoms in designing atom compositions in the final products, e.g. BaTaO_2N modified by different levels of Ca in this work ($\text{BaCa}_{x/3}\text{Ta}_{1-x/3}\text{O}_{2+y}\text{N}_{1-y}$ ($0 \leq x, y \leq 1$)). X-ray powder diffraction patterns (XRD) confirm that all as-prepared samples are single phase compounds (Fig. 1). The patterns are all similar except a slight shift of diffraction peaks towards high angles on descending x in $\text{BaCa}_{x/3}\text{Ta}_{1-x/3}\text{O}_{2+y}\text{N}_{1-y}$, implying unit cell expansions in response to Ca uptake. These compounds can be roughly viewed as solid solutions between BaTaO_2N and complex perovskite $\text{BaCa}_{1/3}\text{Ta}_{2/3}\text{O}_3$ as they share similar crystal structures (space group $Pm\bar{3}m$) [23,59]. Rietveld refinement of XRD data using space group $Pm\bar{3}m$ and under constraints that Ca/Ta, O/N occupy the same crystallographic positions converges with reasonable goodness-of-fit parameters (R_p , R_{wp} and χ^2). Thereby, random distributions of these ions in the perovskite structure are expected. Nevertheless, local ordering or *cis*-type N-Ta-N chains in the structure are still possible [23]. Typical refined XRD patterns for $x = 0.8$ and schematic crystal structures are illustrated in Fig. 2. The refined unit cell parameters are tabulated in Table S1 which agrees well with previous expectations that unit cell slightly expands upon Ca inserting. The nitrogen content for as-prepared samples was determined by thermogravimetric analysis (Table S2) [60–62]. The nitrogen content in the sample rapidly decreases upon Ca insertion, presumably due to a charge compensation phenomenon ($\text{Ca}'_{\text{Ta}} + 3\text{O}'_{\text{N}}$) [63].

3.2. Microstructures

The morphologies of as-prepared sample powders were inspected under field emission scanning electron microscopy (FESEM) conditions. The particle size of sample powders generally decreases with increasing Ca content, implying that Ca helps to inhibit particle growth (Fig. 3). For instance, pristine BaTaO_2N ($x = 0.0$) powders are composed of large particles up to microns while only small granules of a few hundred nanometers are noticed at high doping levels. More importantly, there is a clear sharpening of particle edges at high doping level, in particular,

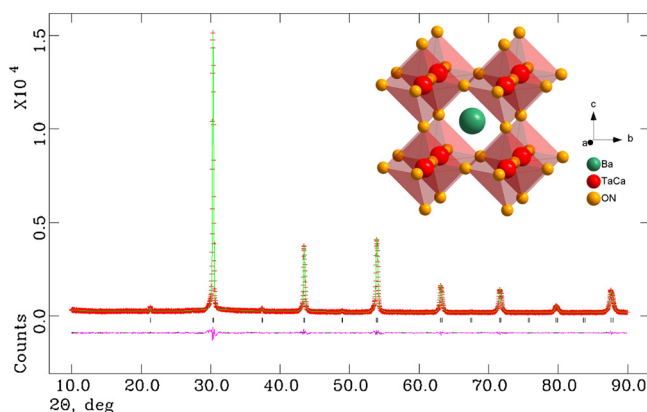


Fig. 2. Observed and calculated X-ray powder diffraction patterns of $\text{BaCa}_{0.1}\text{Ta}_{0.9}\text{O}_{2+y}\text{N}_{1-y}$ ($x = 0.3$). The refinement converged with good R -factors ($R_p = 6.1\%$, $R_{wp} = 4.5\%$, $\chi^2 = 1.284$). Refined crystal structure is schematically shown as inserted image.

at $x = 0.4$, cube-like particles can be easily identified (Fig. 3d and Figure S1d). Thereby, introducing Ca not only helps to control particle sizes but also favors exposure of some crystal facets.

3.3. UV-vis spectra

The color of sample powders shows a clear dependence on Ca levels: the dark red color of pristine BaTaO_2N ($x = 0.0$) is gradually brightened with increasing Ca levels up to $x = 0.4$, after which the color turns to brown, then dark green and finally to light green at $x = 1.0$ (Fig. 3, inserted digital photograph). Such huge color variations suggest substantial alterations in visible light absorption. This is confirmed by their UV-vis absorption spectra (Fig. 4). Pristine BaTaO_2N ($x = 0.0$) exhibit strong light absorbance in the visible light region with absorption edge as far as 660 nm. Its dark hue probably arises from the high absorption tail above 660 nm, which has frequently assigned to various types of defects (e.g. Ta^{4+} species) [64–66]. The effect of introducing Ca to BaTaO_2N is clearly manifested by the blue-shift of the absorption edge. This phenomenon can be rationalized by the diminished nitrogen content along with Ca incorporation as N/O ratios roughly govern the position of valence band edge [40,47]. It can be also verified by comparing $\text{BaCa}_{1/3}\text{Ta}_{2/3}\text{O}_{2.97}\text{N}_{0.03}$ ($x = 1.0$) with its oxide counterpart $\text{BaCa}_{1/3}\text{Ta}_{2/3}\text{O}_3$. The absorption edge of $\text{BaCa}_{1/3}\text{Ta}_{2/3}\text{O}_3$ shifts more than 200 nm (below 300 nm to 500 nm) after introducing merely 1% nitrogen at the oxygen site. Band gap of all samples were then determined by Kubelka-Munk transformation of diffuse reflectance data and extrapolating the absorption edge down to the energy axis. The results are tabulated in Table S1. The gradual enlargement of band gap values along with Ca modification is confirmed. It is worth mentioning that the absorption tail above 660 nm is effectively depressed with x increasing from 0.0 to 0.4, being responsible for the brightened red color. Nevertheless, further increasing Ca level substantially enhances the absorption tail which accounts for the brown and dark green appearance of sample powders. Therefore, by partially substituting Ta with Ca in BaTaO_2N , we managed to gain control over the band gap value and defects levels.

3.4. X-ray photoelectron spectra

The surface conditions of all sample powders were then examined using XPS techniques. The binding energies of core-level electrons for the constituent elements are analyzed and XPS spectra are plotted in Fig. 5. The energy scale has been adjusted according to the adventitious C 1s peak centered at 284.7 eV [67]. Overlapping peaks have been unfolded by applying different Gaussian functions. The Ta 4f signal of pristine BaTaO_2N ($x = 0.0$) reveals a broad hump which can be fitted

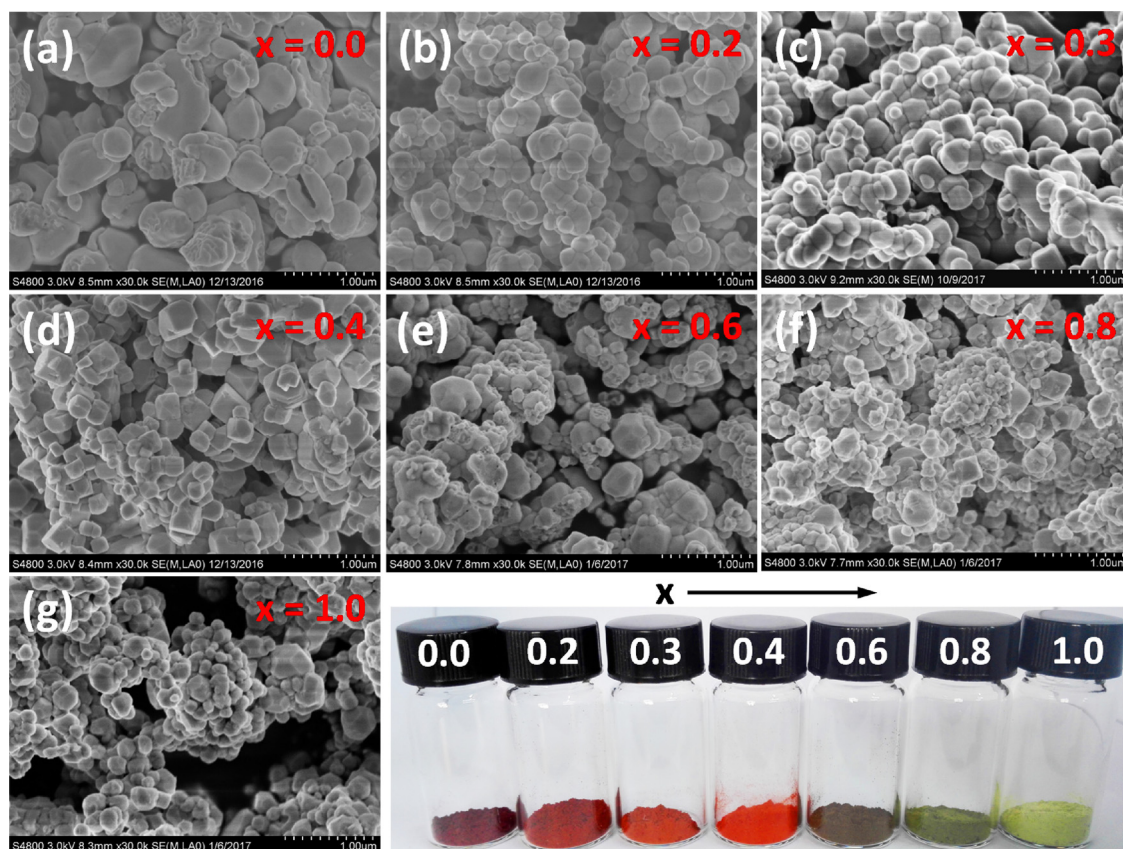


Fig. 3. Field emission scanning electron microscopy images of samples $\text{BaCa}_{x/3}\text{Ta}_{1-x/3}\text{O}_{2+y}\text{N}_{1-y}$ ($0 \leq x, y \leq 1$): (a) $x = 0.0$; (b) $x = 0.2$; (c) $x = 0.3$; (d) $x = 0.4$; (e) $x = 0.6$; (f) $x = 0.8$; (g) $x = 1.0$, a digital photo of sample powders are shown at the bottom.

by four peaks centered around 24.0 eV, 25.2 eV, 26.1 eV and 27.2 eV. These peaks can be assigned to $4f_{5/2}$ and $4f_{7/2}$ state of Ta^{4+} and Ta^{5+} species [68,69], confirming the existence of large amounts of Ta^{4+} defects in pristine BaTaO_2N ($x = 0.0$). Ta^{4+} species have been recognized as charge recombination centers for photo-generated charges and are detrimental to the photocatalytic activity [64]. Introducing Ca, however, effectively removes Ta^{4+} defects as peaks around 24.0 eV and 26.1 eV disappear at $x \geq 0.3$. This observation is consistent with previous UV–vis spectra that Ca helps to control defects levels. Nonetheless, the underlying mechanism for this improvement is not clear but might be explained by the inductive effect of Ca towards Ta–O(N) bond [70]: Ca^{2+} is more electropositive or electron donating than Ta^{5+} , thereby partially replacing Ta^{5+} with Ca^{2+} helps to increase the level of covalency between remaining Ta^{5+} and $\text{O}^{2-}(\text{N}^{3-})$, which in turn,

stabilize Ta^{5+} in the structure. The O 1s state generally reveals two overlapping peaks centered at 529.7 eV and 531.2 eV, assignable to lattice oxygen (O^{2-}) and surface OH groups [71–83]. A clear increase of latter peaks can be noticed at high Ca levels, indicating that the surface of sample powders becomes more hydrophilic in response to Ca introduction. The N 1s state of all samples exhibit a single weak peak around 395.4 eV and is attributed to surface nitrogen species (e.g. NH_2 , etc.) [20,84]. The absence of lattice N^{3-} signals is probably due to the detecting limit of XPS techniques that collect information a few nanometers thick at the top surface [67]. The Ca 2p state is poorly resolved at low Ca content and a broad peak centered at 346.9 eV emerges at $x \geq 0.8$, which is ascribed to $2p_{3/2}$ of Ca^{2+} species [85].

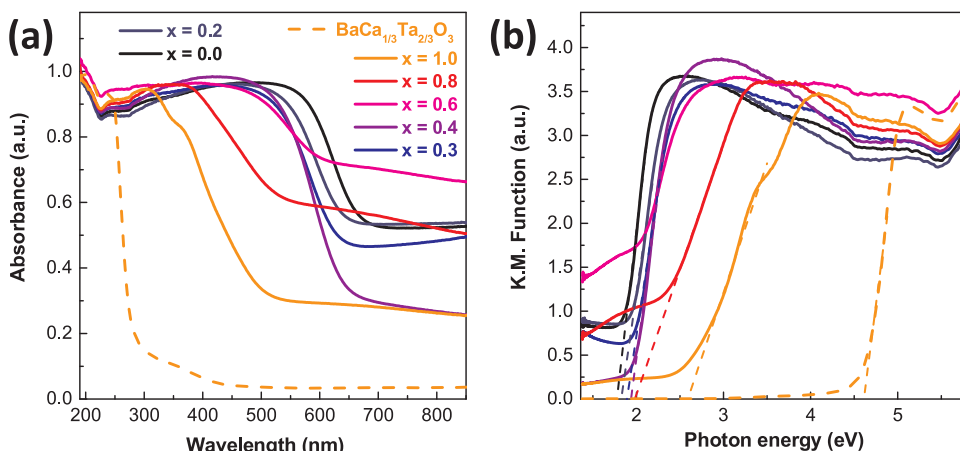


Fig. 4. (a) UV–vis light absorption spectra (converted from diffuse reflectance spectra) of as-prepared sample powders $\text{BaCa}_{x/3}\text{Ta}_{1-x/3}\text{O}_{2+y}\text{N}_{1-y}$ ($0 \leq x, y \leq 1$), $\text{BaCa}_{1/3}\text{Ta}_{2/3}\text{O}_3$ oxide is also included for comparisons; (b) Kubelka-Munk transformation of diffuse reflectance data, band gap values are determined by extrapolating the linear part down to the energy axis.

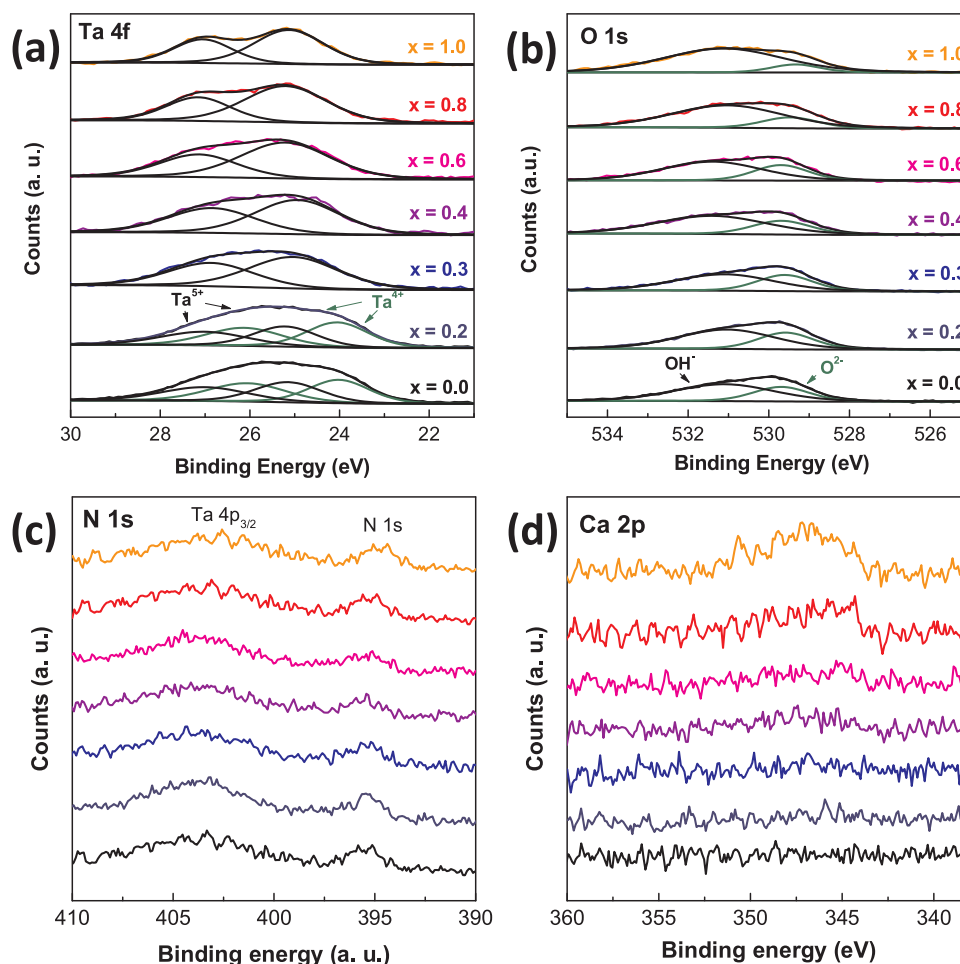


Fig. 5. X-ray photoelectron spectra of freshly prepared samples $\text{BaCa}_{x/3}\text{Ta}_{1-x/3}\text{O}_{2+y}\text{N}_{1-y}$ ($0 \leq x, y \leq 1$): (a) Ta 4f state, (b) O 1s state, (c) N 1s state and (d) Ca 2p state, respectively.

3.5. Photocatalytic water oxidation

The photocatalytic performance of Ca modified BaTaO_2N were evaluated by monitoring their oxygen evolution under visible light illumination ($\lambda \geq 420$ nm). Silver nitrate aqueous solution (0.05 M) was applied as an electron scavenger and 2 wt% CoO_x was loaded as a co-catalyst to promote oxidation reactions. The results are summarized in Fig. 6. It can be realized from the Fig. 6a that pristine BaTaO_2N ($x = 0.0$) demonstrates a relatively poor photocatalytic activity albeit it has the strongest visible light absorbance among the whole series. This observation is consistent with previous reports on BaTaO_2N [31,35]. More importantly, continuous nitrogen evolution was also detected during the whole experiment, indicating the occurrence of photocatalytic self-decomposition in BaTaO_2N . However, efficient photocatalytic water oxidation was realized in Ca modified samples. For instance, nearly 3-fold enhancement in oxygen evolution was achieved in $\text{BaCa}_{0.10}\text{Ta}_{0.90}\text{O}_{2.27}\text{N}_{0.73}$ ($x = 0.3$) under the same conditions as pristine BaTaO_2N . Moreover, photocatalytic self-decomposition events were considerably inhibited as nitrogen evolution was effectively quenched after first hour illumination at $x = 0.3$. Such a large improvement over photocatalytic activity and stability by Ca modification is much more striking compared to other doping schemes or morphology engineering [31,32,35], highlighting a tangible strategy to realize efficient photocatalytic water splitting on BaTaO_2N . Nevertheless, introducing high level of Ca ($x \geq 0.4$) to the structure of BaTaO_2N has negative effects to both photocatalytic activity and stability, probably due to rapid descending of visible light absorbance and ascending of defects levels in these samples as has been revealed by UV-vis spectra (Fig. 4). The

abnormal points at $x = 0.4$ and $x = 0.6$ are probably associated with the stability of these two compounds. For instance, the better performance of sample $x = 0.6$ might be due to the instability of this sample whereby self-sacrificial phenomenon takes place (Fig. 6b). The photocatalytic water oxidation reactions on $\text{BaCa}_{0.10}\text{Ta}_{0.90}\text{O}_{2.27}\text{N}_{0.73}$ ($x = 0.3$) were further studied by altering the amounts of CoO_x loaded and under monochromatic light illumination. An optimal loading point of CoO_x at 2 wt% was observed for this sample whilst the activity decreased sharply when deviating this point. The apparent quantum efficiency (AQE) of $\text{BaCa}_{0.10}\text{Ta}_{0.90}\text{O}_{2.27}\text{N}_{0.73}$ ($x = 0.3$) for photocatalytic water oxidation was then determined under monochromatic light illumination (Fig. 6d). An AQE as high as $\sim 2.1\%$ was achieved at 420 ± 20 nm which stands as the highest AQE for BaTaO_2N reported to date. The AQE at different monochromatic light agrees well with the absorption curve of $\text{aCa}_{0.10}\text{Ta}_{0.90}\text{O}_{2.27}\text{N}_{0.73}$ ($x = 0.3$), confirming real photocatalytic processes. It is worth pointing out that AQE accounts for the minimum limit of the real quantum efficiency as we include all photons for calculation and disregard the reflection losses.

3.6. Photoelectrochemical (PEC) analysis

For better understanding the origin of improved photocatalytic activity over Ca modified BaTaO_2N as well as to gain some insights into the critical role of CoO_x cocatalyst, we have performed photoelectrochemical (PEC) analysis on photoelectrodes fabricated from sample powders. First, liner sweep voltammetry (LSV) under chopped light illumination was carried out and the results for $\text{BaCa}_{0.10}\text{Ta}_{0.90}\text{O}_{2.27}\text{N}_{0.73}$ ($x = 0.3$) and pristine BaTaO_2N ($x = 0.0$) are summarized in Fig. 7a

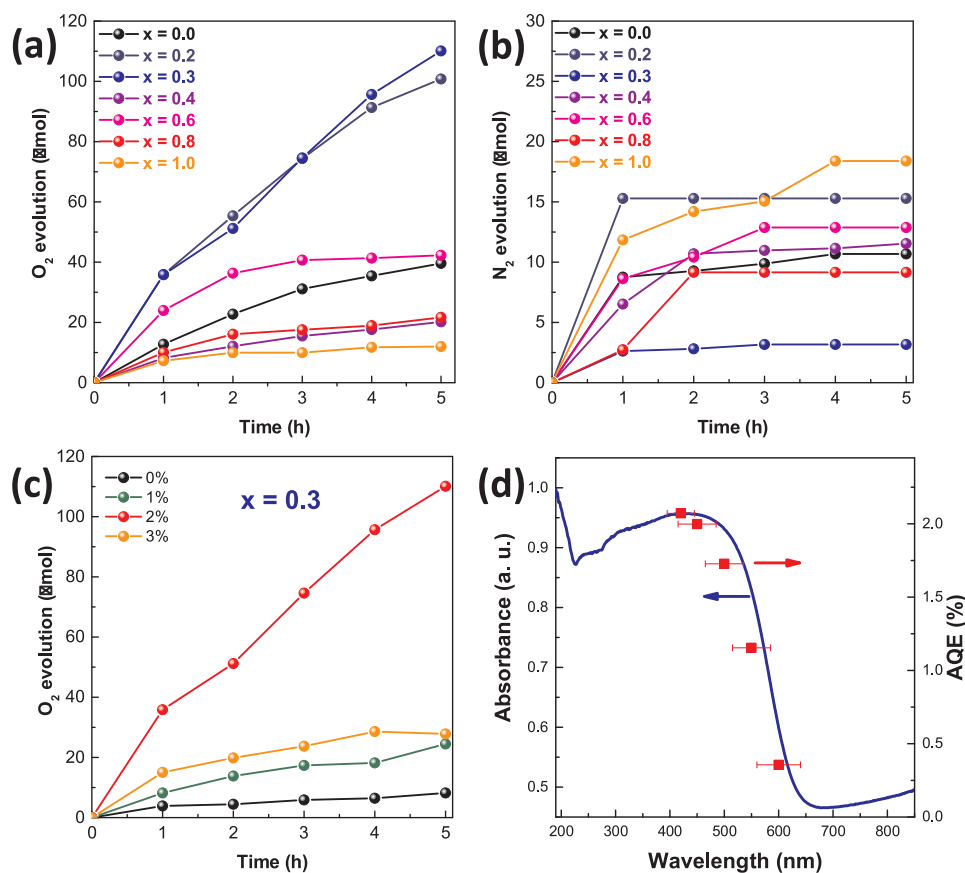


Fig. 6. (a) Temporal photocatalytic oxygen evolution of as-prepared samples $\text{BaCa}_{x/3}\text{Ta}_{1-x/3}\text{O}_{2+y}\text{N}_{1-y}$ ($0 \leq x, y \leq 1$) under visible light illumination ($\lambda \geq 420$ nm), 2 wt% CoO_2 was loaded as a cocatalyst; (b) concomitant nitrogen evolution during photocatalytic oxygen evolution reactions; (c) temporal photocatalytic oxygen evolution of $\text{BaCa}_{0.10}\text{Ta}_{0.90}\text{O}_{2.27}\text{N}_{0.73}$ ($x = 0.3$) loaded with different amounts of CoO_2 under visible light illumination; (d) action spectra (apparent quantum efficiency (AQE) vs excitation wavelength) of $\text{BaCa}_{0.10}\text{Ta}_{0.90}\text{O}_{2.27}\text{N}_{0.73}$ ($x = 0.3$), 2 wt% CoO_2 was loaded as a cocatalyst and monochromatic light was generated by filtering the output of lamp using bandpass filters.

and b. It is clear from Fig. 7a that Ca modification has a positive role in extracting photocurrent from sample powders. The photocurrent for $\text{BaCa}_{0.10}\text{Ta}_{0.90}\text{O}_{2.27}\text{N}_{0.73}$ ($x = 0.3$) is roughly 3-fold higher than pristine BaTaO_2N ($x = 0.0$), being consistent with their photocatalytic activities. Such a large enhancement in photocurrent stems probably from the improvements of intrinsic charge separation conditions as both samples share almost identical onset potential for photocurrent (~ 0.0 V vs RHE). This is also verified by their flat band potentials (V_{fb}) determined from Mott-Schottky (MS) analysis (Figure S2). $\text{BaCa}_{0.10}\text{Ta}_{0.90}\text{O}_{2.27}\text{N}_{0.73}$ ($x = 0.3$) owns a close V_{fb} to BaTaO_2N ($x = 0.0$) thereby its higher photocurrent is not due to a stronger electric field induced in the depletion layer that enhances the separation of photo-generated charges. Band edge positions of both compounds are then determined according to MS results and are illustrated in Figure S2b. $\text{BaCa}_{0.10}\text{Ta}_{0.90}\text{O}_{2.27}\text{N}_{0.73}$ ($x = 0.3$) owns a more positive valence band edge position than pristine BaTaO_2N ($x = 0.0$), probably being another reason for the better photocatalytic water oxidation activity. However, MS curve of $\text{BaCa}_{0.10}\text{Ta}_{0.90}\text{O}_{2.27}\text{N}_{0.73}$ ($x = 0.3$) reveals a much larger slope than the one for BaTaO_2N ($x = 0.0$), which suggests a much lower donor concentration according to MS equation [86]:

$$\frac{1}{C^2} = \frac{2}{\epsilon\epsilon_0 A^2 e N_D} (V - V_{fb} - \frac{k_B T}{e}) \quad (1)$$

where C and A are the interfacial capacitance and area, respectively, V the electrical bias applied, k_B is Boltzmann's constant, N_D the donor concentration, T the absolute temperature, ϵ the dielectric constant, and e is the electronic charge. Considering the strong XPS signals for Ta^{4+} species in pristine BaTaO_2N ($x = 0.0$), the donors are most likely Ta^{4+} defects (*i.e.* Ta_{Ta}^{4+}). These charged defects prefer to trap photo-generated charges and often act as efficient charge recombination centers that are responsible for poor photocatalytic activity. Therefore, the higher photocatalytic activity in Ca modified BaTaO_2N can be ascribed to the reduction of Ta^{4+} species in the material. On the other hand, switching

the illumination conditions from visible light to AM 1.5 induces only mild increase in the photocurrent (Fig. 7b), suggesting that the photocatalytic activity of these samples is governed mainly by visible light photons. We then perform LSV on $\text{BaCa}_{0.10}\text{Ta}_{0.90}\text{O}_{2.27}\text{N}_{0.73}$ ($x = 0.3$) loaded with different amounts of CoO_2 . The results are illustrated in Fig. 7c. Plain $\text{BaCa}_{0.10}\text{Ta}_{0.90}\text{O}_{2.27}\text{N}_{0.73}$ (0.0 wt% CoO_2 loading) displays negligible photocurrent under visible light illumination even with a large electrical bias, implying that the surface of $\text{BaCa}_{0.10}\text{Ta}_{0.90}\text{O}_{2.27}\text{N}_{0.73}$ is inert for water oxidation reactions. This is supported by a large charge transfer resistance in its impedance spectra (Fig. 7d). Loading CoO_2 effectively reduces the charge transfer resistance, resulting in the large photocurrent observed. The optimal loading point of CoO_2 at 2 wt% is manifested by the smallest charge transfer resistance as well as the largest photocurrent in LSV.

Intuitive questions arise as how defects such as Ta^{4+} influence photo-generated charges and CoO_2 contributes to the transfer of these charges. We then carried out open-circuit voltage decay (OCVD) measurements on sample $\text{BaCa}_{0.10}\text{Ta}_{0.90}\text{O}_{2.27}\text{N}_{0.73}$ ($x = 0.3$) and pristine BaTaO_2N ($x = 0.0$). OCVD measurements refer to the voltage change of sample photoelectrode at open-circuit condition in response to light illumination and termination [38,87,88]. For n-type semiconductor photoelectrode, light illumination under open-circuit condition accumulates electrons in the sample as holes are driven to the surface and are consumed by water oxidation reactions [89]. This effectively decreases the open-circuit voltage (V_{oc}) of photoelectrode due to negative shift of Fermi level in the sample. Steady V_{oc} approaches as long as electron accumulation is counterbalanced by various electron dissipation events (e.g. recombined with trapped holes). Likewise, terminating light illumination leads to decay of V_{oc} to the value in the dark which is governed by those electron dissipation events. Thereby, V_{oc} decay processes give a direct evaluation of charge separation and recombination situations in the semiconductor. The lifetime of those accumulated electrons can be quantitatively approximated using the

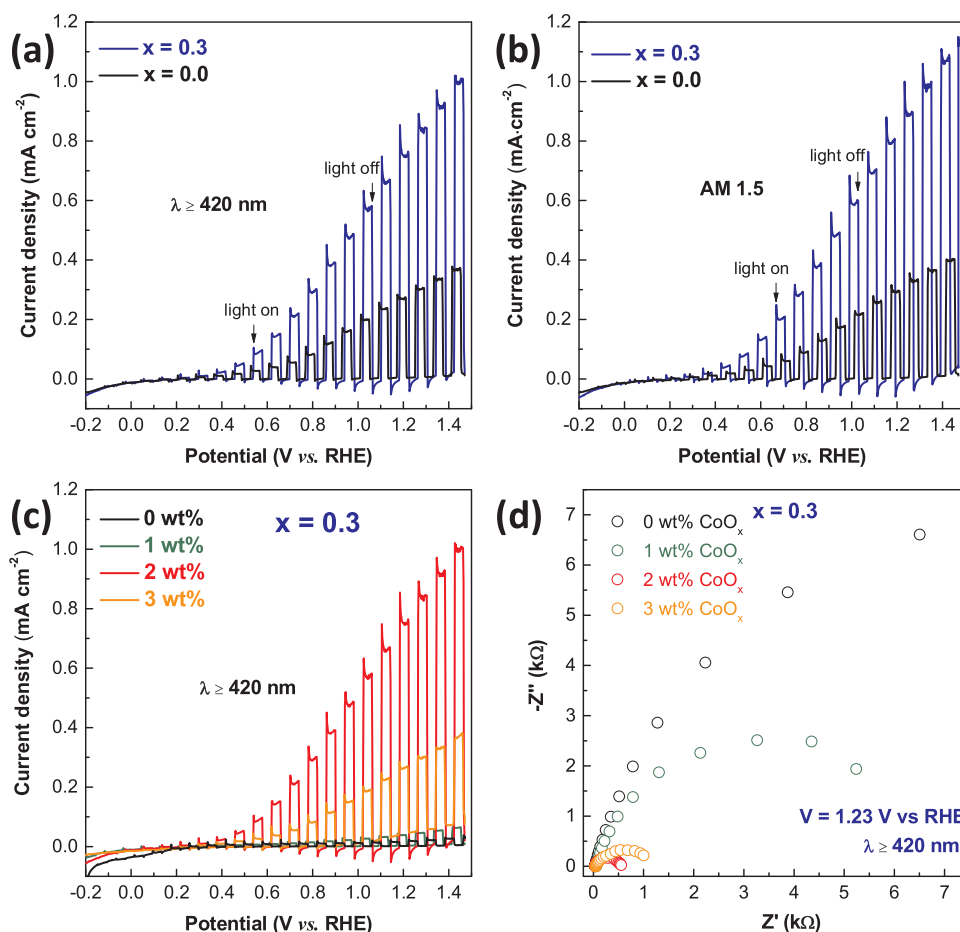


Fig. 7. Linear sweep voltammetry (LSV) of photoelectrodes prepared from sample BaCa_{0.10}Ta_{0.90}O_{2.27}N_{0.73} ($x = 0.3$) and pristine BaTaO₂N ($x = 0.0$) under chopped light illumination: visible light ($\lambda \geq 420$ nm) (a) and AM 1.5 (b); LSV of photoelectrodes for BaCa_{0.10}Ta_{0.90}O_{2.27}N_{0.73} ($x = 0.3$) loaded with different amounts of CoO_x under chopped visible light illumination ($\lambda \geq 420$ nm) (c) and Nyquist plot of impedance spectra for the same electrodes with electrical bias ($V = 1.23$ V vs RHE) under visible light illumination ($\lambda \geq 420$ nm) (d).

following equation [87,88]:

$$\tau_n = \frac{k_B T}{e} \left(\frac{dV_{oc}}{dt} \right)^{-1} \quad (2)$$

where τ_n is potential dependent lifetime, k_B is Boltzmann's constant, T is the temperature in K and e is the elementary charge. Fig. 8a illustrates the OCVD results of BaCa_{0.10}Ta_{0.90}O_{2.27}N_{0.73} ($x = 0.3$) and pristine BaTaO₂N ($x = 0.0$) without CoO_x loading in Ar atmosphere. It is clear from Fig. 8a that BaCa_{0.10}Ta_{0.90}O_{2.27}N_{0.73} ($x = 0.3$) owns much slower V_{oc} decay processes than pristine BaTaO₂N ($x = 0.0$). The decay of V_{oc} for pristine BaTaO₂N is apparent even during the light illumination

period, indicating rapid drainage of photo-generated electrons. The calculated electron lifetime of these two samples are displayed in Fig. 8b. BaCa_{0.10}Ta_{0.90}O_{2.27}N_{0.73} ($x = 0.3$) owns an electron lifetime almost one order of magnitude longer than pristine BaTaO₂N, confirming that the improved photocatalytic activity stems from better charge separation situations after Ca modification. In other words, defects like Ta⁴⁺ strongly promote charge recombination and greatly shorten electron lifetime. These observations are all consistent with previous UV-vis spectra, XPS data and Mott-Schottky analysis.

The OCVD measurements were further performed on

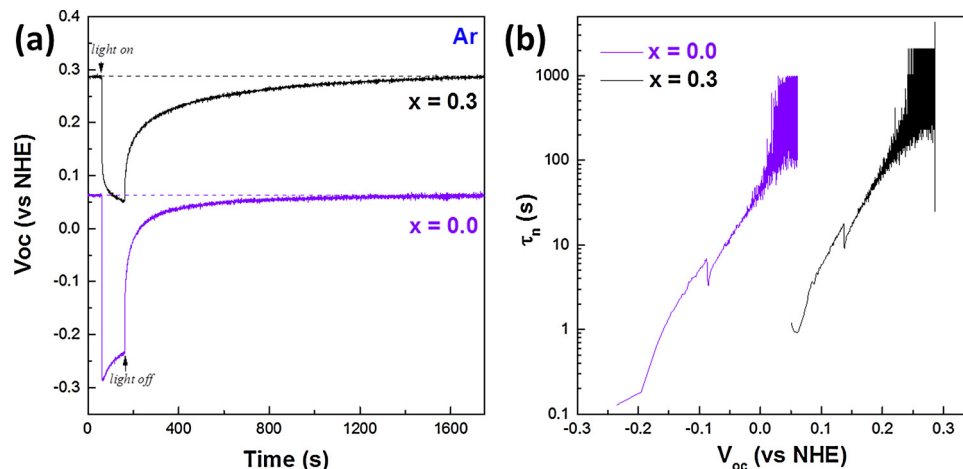


Fig. 8. (a) V_{oc} time profile of BaCa_{0.10}Ta_{0.90}O_{2.27}N_{0.73} ($x = 0.3$) and pristine BaTaO₂N ($x = 0.0$) without CoO_x loading in Ar. Illumination ($\lambda \geq 420$ nm) started after attaining a steady V_{oc} in the dark and terminated after 100 s; (b) the electron lifetime derived from V_{oc} decay curves in (a) according to Eq. 2.

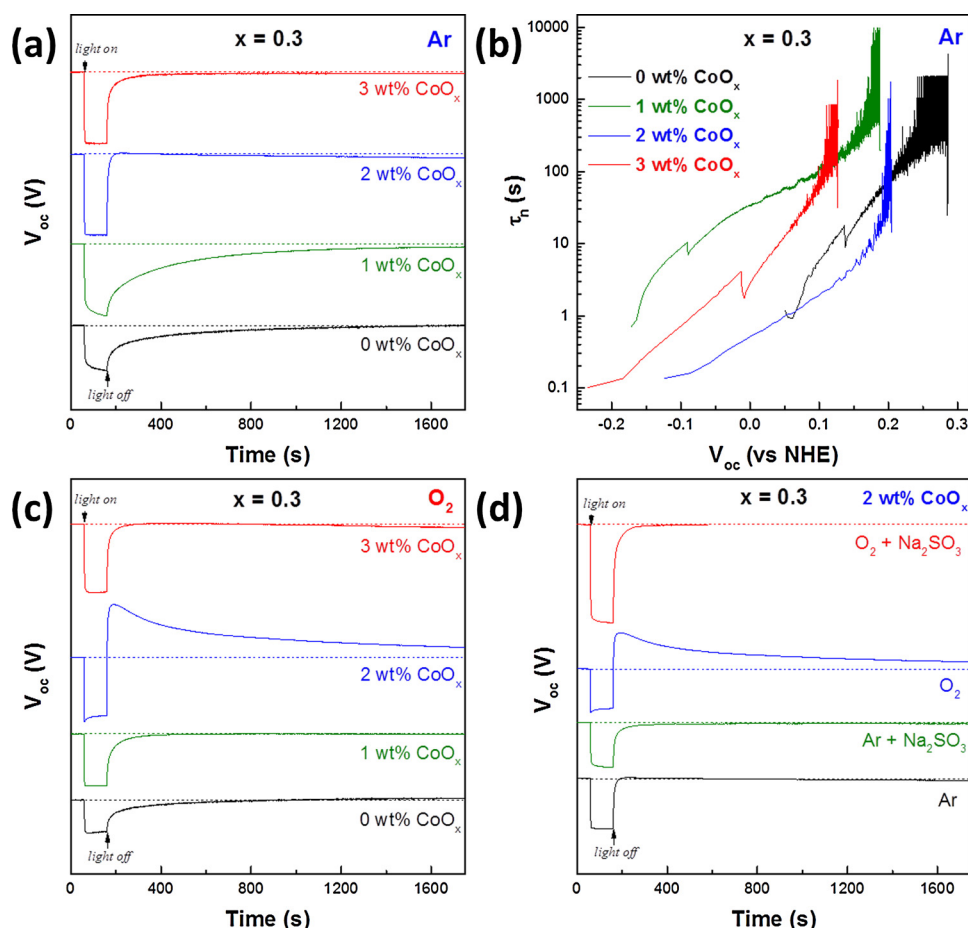


Fig. 9. (a) V_{oc} time profile of BaCa_{0.10}Ta_{0.90}O_{2.27}N_{0.73} (x = 0.3) loaded with different amounts of CoO_x in Ar; (b) the electron lifetime derived from V_{oc} decay curves in (a) according to Eq. 2; (c) V_{oc} time profile of BaCa_{0.10}Ta_{0.90}O_{2.27}N_{0.73} (x = 0.3) loaded with different amounts of CoO_x in O₂; (d) V_{oc} time profile of BaCa_{0.10}Ta_{0.90}O_{2.27}N_{0.73} (x = 0.3) loaded with 2 wt% CoO_x in the presence or absence of Na₂SO₃ in Ar or O₂.

BaCa_{0.10}Ta_{0.90}O_{2.27}N_{0.73} (x = 0.3) loaded with different amounts of CoO_x. The results are illustrated in Fig. 9a. It can be seen from Fig. 9a that loading 1 wt% CoO_x slows down the decay processes of V_{oc} , indicating that charge separation situations are improved. This can be rationalized by the fact that cocatalyst CoO_x serves hole collector, i.e. formation of metal-semiconductor Schottky junction which helps to separate charges and extend electron lifetime (Fig. 9b) [90]. Nevertheless, reverse trend was noticed for further CoO_x loading (2 wt% and 3 wt%) whereby extremely rapid restoration of V_{oc} to the dark value upon light termination can be seen. This phenomenon probably accounts for the back-donating holes from CoO_x to the sample which recombines with accumulated electrons rapidly. In other words, appreciable amounts of holes are collected and stored by CoO_x under light illumination conditions. The storage of holes on CoO_x and back-donating them to the semiconductor was also verified by a series of control experiments. First, OCVD measurements were performed in O₂ saturated conditions (Fig. 9c). O₂ is a product of water oxidation reaction (Eq. (3)). Increasing the level of product in the system inhibits the proceeding of the reactions and slow down the hole consumption.



V_{oc} decay profile in this case was accelerated for all samples compared with those in Ar atmosphere as more holes will be back-donated to the semiconductor. More strikingly, at 2 wt% CoO_x loading, V_{oc} restored to a value more positive than the one in the dark conditions, indicating that considerable amounts of holes were back-donated to the semiconductor. This explanation was further supported by applying hole scavenger Na₂SO₃ to the system which will remove holes stored in CoO_x (Fig. 9d). As can be seen in Fig. 9c, the aforementioned phenomenon in 2 wt% CoO_x loading disappears in the presence of Na₂SO₃ in both O₂ and Ar atmospheres, confirming storage of holes in previous case. It is

worth pointing out that water oxidation reaction is a four-proton-four-hole reaction which requires accumulation holes at single reaction site. Storing significant amounts of holes on CoO_x is undoubtedly beneficial for water oxidation reaction and 2 wt% CoO_x loading works best for this purpose, being the optimal loading point for photocatalytic activities.

4. Conclusions

A series of Ca modified BaTaO₂N (BaCa_{x/3}Ta_{1-x/3}O_{2+y}N_{1-y}, (0 ≤ x, y ≤ 1)) was successfully prepared via a polymerized complex method. The perovskite structures of BaTaO₂N are maintained with slight unit cell expansions along with Ca incorporation. Various important properties such as band gap, defect levels, nitrogen content can be tuned by altering Ca content in the sample. Increasing Ca content generally leads to enlargement of band gap, decrement of defects levels and nitrogen content. More importantly, the photocatalytic activities for water oxidation reactions as well as photocatalytic self-decomposition were significantly improved by Ca modification. Nearly 3-fold enhancement in oxygen evolution was achieved in BaCa_{0.10}Ta_{0.90}O_{2.27}N_{0.73} (x = 0.3) compared to pristine BaTaO₂N. The activity was further optimized by varying the amounts of cocatalyst CoO_x loaded and apparent quantum efficiency approaches as high as ~ 2.1% at 420 ± 20 nm illumination which stands as the highest AQE for BaTaO₂N reported to date. Photoelectrochemical analysis reveals much enhanced photocurrent for water oxidation reaction in Ca modified BaTaO₂N which is associated with low defect levels in the sample. Loading cocatalyst CoO_x serves to reduce charge transfer resistance therefore lowers energy barrier for water oxidation reaction. Open-circuit voltage decay (OCVD) measurements further confirm better charge separation situations in Ca modified BaTaO₂N which accounts for longer electron lifetime compared to pristine one. The function of cocatalyst CoO_x to collect and

store photo-generated holes is also identified. The optimal loading point for cocatalyst CoO_x corresponds to the amounts of CoO_x that give the highest capacity for hole storage.

Acknowledgements

We thank Young Scientists Fund of the National Natural Science Foundation of China (Grant No. 21401142, 51708153) for funding and Recruitment Program of Global Youth Experts (1000 plan). The work was also supported by Shanghai Science and Technology Commission (14DZ2261100) and the Fundamental Research Funds for the Central Universities.

Appendix A. Supplementary data

Supplementary material related to this article can be found, in the online version, at doi:<https://doi.org/10.1016/j.apcatb.2018.06.017>.

References

- [1] N.S. Lewis, D.G. Nocera, P. Natl. Acad. Sci. USA 103 (2006) 15729–15735.
- [2] D.G. Nocera, Chem. Soc. Rev. 38 (2009) 13–15.
- [3] Annual Energy Outlook, U. S. Energy Information Administration (2017) (2017).
- [4] B. Dudley, BP Statistical Rev. World Energy 2016 (June) (2016).
- [5] K. Maeda, K. Teramura, D.L. Lu, T. Takata, N. Saito, Y. Inoue, K. Domen, Nature 440 (2006) 295–295.
- [6] Z.G. Zou, J.H. Ye, K. Sayama, H. Arakawa, Nature 414 (2001) 625–627.
- [7] X.X. Xu, C. Random, P. Efsthathiou, J.T.S. Irvine, Nat. Mater. 11 (2012) 595–598.
- [8] X.C. Wang, K. Maeda, A. Thomas, K. Takanabe, G. Xin, J.M. Carlsson, K. Domen, M. Antonietti, Nat. Mater. 8 (2009) 76–80.
- [9] X.B. Huang, G.X. Zhao, G. Wang, J. Mater. Chem. A 5 (2017) 24631–24635.
- [10] J.A. Turner, Science 305 (2004) 972–974.
- [11] J.A. Turner, Science 285 (1999) 687–689.
- [12] J.R. Bolton, S.J. Strickler, J.S. Connolly, Nature 316 (1985) 495–500.
- [13] X.B. Chen, S.H. Shen, L.J. Guo, S.S. Mao, Chem. Rev. 110 (2010) 6503–6570.
- [14] M.R. Hoffmann, S.T. Martin, W.Y. Choi, D.W. Bahnemann, Chem. Rev. 95 (1995) 69–96.
- [15] G. Zhang, G. Liu, L.Z. Wang, J.T.S. Irvine, Chem. Soc. Rev. 45 (2016) 5951–5984.
- [16] A. Kudo, Y. Miseki, Chem. Soc. Rev. 38 (2009) 253–278.
- [17] Z.B. Chen, T.F. Jaramillo, T.G. Deutsch, A. Kleiman-Shwarsstein, A.J. Forman, N. Gaillard, R. Garland, K. Takanabe, C. Heske, M. Sunkara, E.W. McFarland, K. Domen, E.L. Miller, J.A. Turner, H.N. Dinh, J. Mater. Res. 25 (2010) 3–16.
- [18] J.L. Du, Z.F. Chen, C.C. Chen, T.J. Meyer, J. Am. Chem. Soc. 137 (2015) 3193–3196.
- [19] F.F. Wu, M.L. Lv, X.Q. Sun, Y.H. Xie, H.M. Chen, S. Ni, G. Liu, X.X. Xu, ChemCatChem 8 (2016) 615–623.
- [20] F.F. Wu, G. Liu, X.X. Xu, J. Catal. 346 (2017) 10–20.
- [21] F.F. Wu, X.Q. Sun, G. Liu, X.X. Xu, Catal. Sci. Technol. 7 (2017) 4640–4647.
- [22] A. Fuertes, Mater. Horiz. 2 (2015) 453–461.
- [23] M.H. Yang, J. Oro-Sole, J.A. Rodgers, A.B. Jorge, A. Fuertes, J.P. Attfield, Nat. Chem. 3 (2011) 47–52.
- [24] Y.I. Kim, P.M. Woodward, K.Z. Baba-Kishi, C.W. Tai, Chem. Mater. 16 (2004) 1267–1276.
- [25] M. Ahmed, X.X. Guo, Inorg. Chem. Front. 3 (2016) 578–590.
- [26] A. Fuertes, J. Mater. Chem. 22 (2012) 3293–3299.
- [27] B. Siritanaratkul, K. Maeda, T. Hisatomi, K. Domen, Chemsuschem 4 (2011) 74–78.
- [28] F. Oehler, S.G. Ebbinghaus, Solid State Sci. 54 (2016) 43–48.
- [29] M. Higashi, R. Abe, K. Teramura, T. Takata, B. Ohtani, K. Domen, Chem. Phys. Lett. 452 (2008) 120–123.
- [30] M. Higashi, R. Abe, T. Takata, K. Domen, Chem. Mater. 21 (2009) 1543–1549.
- [31] K. Maeda, K. Domen, Angew. Chem. Int. Ed. 51 (2012) 9865–9869.
- [32] M. Hojamberdiev, K. Yubuta, J.J.M. Vequizo, A. Yamakata, S. Oishi, K. Domen, K. Teshima, Cryst. Growth Des. 15 (2015) 4663–4671.
- [33] C.Z. Wang, T. Hisatomi, T. Minegishi, Q. Wang, M. Zhong, M. Katayama, J. Kubota, K. Domen, J. Phys. Chem. C 120 (2016) 15758–15764.
- [34] K. Ueda, T. Minegishi, J. Clune, M. Nakabayashi, T. Hisatomi, H. Nishiyama, M. Katayama, N. Shibata, J. Kubota, T. Yamada, K. Domen, J. Am. Chem. Soc. 137 (2015) 2227–2230.
- [35] K. Maeda, D.L. Lu, K. Domen, Angew. Chem. Int. Ed. 52 (2013) 6488–6491.
- [36] M. Matsukawa, R. Ishikawa, T. Hisatomi, Y. Moriya, N. Shibata, J. Kubota, Y. Ikumura, K. Domen, Nano Lett. 14 (2014) 1038–1041.
- [37] A.E. Maegli, E.H. Otal, T. Hisatomi, S. Yoon, C.M. Leroy, N. Schauble, Y. Lu, M. Gratzel, A. Weidenkaff, Emrs Symposium T: Materials for Solar Hydrogen Via Photo-Electrochemical Production 22 (2012), pp. 61–66.
- [38] Y.H. Xie, Y.W. Wang, Z.F. Chen, X.X. Xu, Chemsuschem 9 (2016) 1403–1412.
- [39] A. Kasahara, K. Nukumizu, G. Hitoki, T. Takata, J.N. Kondo, M. Hara, H. Kobayashi, K. Domen, J. Phys. Chem. A 106 (2002) 6750–6753.
- [40] M. Jansen, H.P. Letschert, Nature 404 (2000) 980–982.
- [41] Z.H. Pan, T. Hisatomi, Q. Wang, S.S. Chen, M. Nakabayashi, N. Shibata, C.S. Pan, T. Takata, M. Katayama, T. Minegishi, A. Kudo, K. Domen, ACS Catal. 6 (2016) 7188–7196.
- [42] Q. Wang, Y.B. Li, T. Hisatomi, M. Nakabayashi, N. Shibata, J. Kubota, K. Domen, J. Catal. 328 (2015) 308–315.
- [43] Q. Wang, T. Hisatomi, Y. Suzuki, Z.H. Pan, J. Seo, M. Katayama, T. Minegishi, H. Nishiyama, T. Takata, K. Seki, A. Kudo, T. Yamada, K. Domen, J. Am. Chem. Soc. 139 (2017) 1675–1683.
- [44] A. Kudo, Mrs. Bull. 36 (2011) 32–38.
- [45] O. Khaselev, J.A. Turner, Science 280 (1998) 425–427.
- [46] G. Tobias, E. Canadell, J. Am. Chem. Soc. 128 (2006) 4318–4329.
- [47] S. Balaz, S.H. Porter, P.M. Woodward, L.J. Brinson, Chem. Mater. 25 (2013) 3337–3343.
- [48] Y.I. Kim, P.M. Woodward, J. Solid State Chem. 180 (2007) 3224–3233.
- [49] K. Hibino, M. Yashima, T. Oshima, K. Fujii, K. Maeda, Dalton T. 46 (2017) 14947–14956.
- [50] B.B. Dong, Y. Qi, J.Y. Cui, B.D. Liu, F.Q. Xiong, X. Jiang, Z. Li, Y.J. Xiao, F.X. Zhang, C. Li, Dalton T. 46 (2017) 10707–10713.
- [51] K. Maeda, K. Domen, J. Catal. 310 (2014) 67–74.
- [52] A.C. Larson, R.B. Von Dreele, Los Alamos National Laboratory Report No. LA-UR-86-748, (1994).
- [53] G. Kortum, W. Braun, G. Herzog, Angew. Chem. Int. Ed. 2 (1963) 333–341.
- [54] P.Vd. Heide, X-Ray Photoelectron Spectroscopy—An Introduction to Principles and Practices, John Wiley & Sons, Inc, Hoboken, 2012.
- [55] S.S. Chen, S. Shen, G.J. Liu, Y. Qi, F.X. Zhang, C. Li, Angew. Chem. Int. Ed. 54 (2015) 3047–3051.
- [56] Y.W. Wang, D.Z. Zhu, X.X. Xu, Acs Appl. Mater. Int. 8 (2016) 35407–35418.
- [57] Y.J. Zhong, Z.S. Li, X. Zhao, T. Fang, H.T. Huang, Q.F. Qian, X.F. Chang, P. Wang, S.C. Yan, Z.T. Yu, Z.G. Zou, Adv. Funct. Mater. 26 (2016) 7156–7163.
- [58] W.D. Kingery, H.K. Bowen, D.R. Uhlmann, Introduction to Ceramics, John Wiley & Sons, Inc, New York, 1975.
- [59] F. Galasso, J.R. Barranté, L. Katz, J. Am. Chem. Soc. 83 (1961) 2830–2832.
- [60] D. Logvinovich, A. Borger, M. Dobeli, S.G. Ebbinghaus, A. Reller, A. Weidenkaff, Prog. Solid State (2007) 281–290 Ch 35.
- [61] R. Aguiar, D. Logvinovich, A. Weidenkaff, A. Reller, S.G. Ebbinghaus, Thermochim. Acta 471 (2008) 55–60.
- [62] A. Rachel, S.G. Ebbinghaus, M. Gungerich, P.J. Klar, J. Hanss, A. Weidenkaff, A. Reller, Thermochim. Acta 438 (2005) 134–143.
- [63] F. Chevre, F. Tessier, R. Marchand, Eur. J. Inorg. Chem. (2006) 1223–1230.
- [64] T. Matoba, K. Maeda, K. Domen, Chem.-Eur. J. 17 (2011) 14731–14735.
- [65] K. Maeda, N. Nishimura, K. Domen, Appl. Catal. A-Gen. 370 (2009) 88–92.
- [66] K. Maeda, M. Higashi, D.L. Lu, R. Abe, K. Domen, J. Am. Chem. Soc. 132 (2010) 5858–5868.
- [67] P. Van der Heide, X-Ray Photoelectron Spectroscopy - An Introduction to Principles and Practices, John Wiley & Sons, Inc, Hoboken, New Jersey, 2012.
- [68] M.V. Ivanov, T.V. Perevalov, V.S. Aliev, V.A. Gritsenko, V.V. Kaichev, J. Appl. Phys. (2011) 110.
- [69] X. Yu, W. Li, Z.H. Li, J.W. Liu, P.A. Hu, Appl. Catal. B-Environ. 217 (2017) 48–56.
- [70] J. Etourneau, J. Portier, F. Menil, J. Alloy Compd. 188 (1992) 1–7.
- [71] M.L. Lv, X.Q. Sun, S.H. Wei, C. Shen, Y.L. Mi, X.X. Xu, Acs Nano 11 (2017) 11441–11448.
- [72] H.M. Chen, X.X. Xu, Appl. Catal. B-Environ. 206 (2017) 35–43.
- [73] L. Jiang, S. Ni, G. Liu, X.X. Xu, Appl. Catal. B-Environ. 217 (2017) 342–352.
- [74] L.W. Lu, M.L. Lv, D. Wang, G. Liu, X.X. Xu, Appl. Catal. B-Environ. 200 (2017) 412–419.
- [75] X.Q. Sun, X.X. Xu, Appl. Catal. B-Environ. 210 (2017) 149–159.
- [76] R.N. Wang, S. Ni, G. Liu, X.X. Xu, Appl. Catal. B-Environ. 225 (2018) 139–147.
- [77] L.W. Lu, M.L. Lv, G. Liu, X.X. Xu, Appl. Surf. Sci. 391 (2017) 535–541.
- [78] X.Q. Sun, S.W. Wang, C. Shen, X.X. Xu, ChemCatChem 8 (2016) 2289–2295.
- [79] H.M. Chen, X.Q. Sun, X.X. Xu, Electrochim. Acta 252 (2017) 138–146.
- [80] X.Q. Sun, Y.H. Xie, F.F. Wu, H.M. Chen, M.L. Lv, S. Ni, G. Liu, X.X. Xu, Inorg. Chem. 54 (2015) 7445–7453.
- [81] L.W. Lu, S. Ni, G. Liu, X.X. Xu, Int. J. Hydrogen Energ. 42 (2017) 23539–23547.
- [82] X.X. Xu, Y.H. Xie, S. Ni, A.K. Azad, T.C. Cao, J. Solid State Chem. 230 (2015) 95–101.
- [83] X.X. Xu, M.L. Lv, X.Q. Sun, G. Liu, J. Mater. Sci. 51 (2016) 6464–6473.
- [84] S.S. Chen, J.X. Yang, C.M. Ding, R.G. Li, S.Q. Jin, D.E. Wang, H.X. Han, F.X. Zhang, C. Li, J. Mater. Chem. A 1 (2013) 5651–5659.
- [85] T. Hanawa, M. Ota, Biomaterials 12 (1991) 767–774.
- [86] K. Gelderman, L. Lee, S.W. Donne, J. Chem. Educ. 84 (2007) 685–688.
- [87] B.H. Meekins, P.V. Kamat, Acs Nano 3 (2009) 3437–3446.
- [88] A. Zaban, M. Greenshtein, J. Bisquet, Chemphyschem 4 (2003) 859–864.
- [89] J.A. Turner, J. Chem. Educ. 60 (1983) 327–329.
- [90] D.E. Aspnes, A. Heller, J. Phys. Chem. 87 (1983) 4919–4929.